

A “Seawater-in-Sludge” approach for capacitive biochar production via the alkaline and alkaline earth metals activation

Xiling Li¹, Tianwei Hao (✉)², Yuxin Tang³, Guanghao Chen^{1,4,5,6}

¹ Department of Civil & Environmental Engineering, The Hong Kong University of Science and Technology, Hong Kong 999077, China

² Department of Civil and Environmental Engineering, Faculty of Science and Technology, University of Macao, Macao 999078, China

³ Institute of Applied Physics and Materials Engineering, University of Macao, Macao 999078, China

⁴ Water Technology Center, The Hong Kong University of Science and Technology, Hong Kong 999077, China

⁵ Hong Kong Branch of Chinese National Engineering Research Center for Control & Treatment of Heavy Metal Pollution, The Hong Kong University of Science and Technology, Hong Kong 999077, China

⁶ Wastewater Treatment Laboratory, FYT Graduate School, The Hong Kong University of Science and Technology, Guangzhou 511458, China

HIGHLIGHTS

- Capacitive biochar was produced from sewage sludge.
- Seawater was proved to be an alternative activation agent.
- Minerals vaporization increased the surface area of biochar.
- Molten salts acted as natural templates for the development of porous structure.

ARTICLE INFO

Article history:

Received 4 February 2020

Revised 25 April 2020

Accepted 21 May 2020

Available online 9 July 2020

Keywords:

Sewage sludge

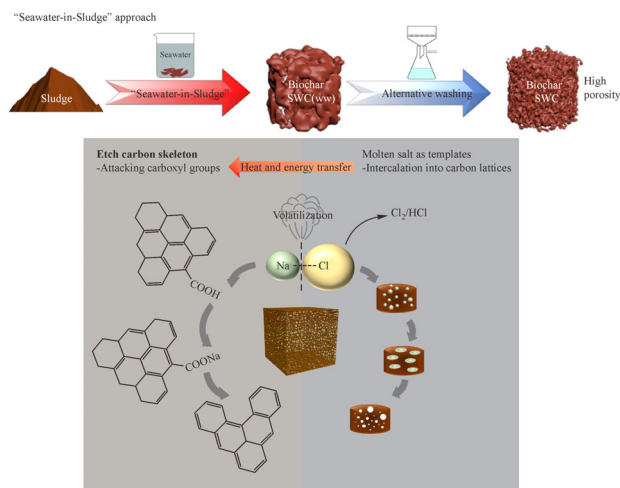
Biochar

Seawater

Recourse recovery

Capacitor

GRAPHIC ABSTRACT



ABSTRACT

Sewage sludge is a potential precursor for biochar production, but its effective utilization involves costly activation steps. To modify biochar properties while ensuring cost-effectiveness, we examined the feasibility of using seawater as an agent to activate biochar produced from sewage sludge. In our proof-of-concept study, seawater was proven to be an effective activation agent for biochar production, achieving a surface area of 480.3 m²/g with hierarchical porosity distribution. Benefited from our design, the catalytic effect of seawater increased not only the surface area but also the graphitization degree of biochar when comparing the pyrolysis of sewage sludge without seawater. This leads to seawater activated biochar electrodes with lower resistance, higher capacitance of 113.9 F/g comparing with control groups without seawater. Leveraging the global increase in the salinity of groundwater, especially in coastal areas, these findings provide an opportunity for recovering a valuable carbon resource from sludge.

© Higher Education Press 2020

1 Introduction

Waste activated sludge (WAS) from wastewater treatment plants (WWTPs) continues to present a challenge globally. Recovery of various useful carbon resources (e.g., enzymes, bio-plastics, bio-pesticides, proteins) beyond biogas from WAS may offer a new economic incentive for WWTPs. In recent years, the slow pyrolysis of WAS to produce biochar while reducing sludge treatment and disposal cost has attracted attention (Cao and Pawłowski, 2012). The process contributes to global carbon sequestration via biochar production as a carbon sink (Lee et al., 2010). Unlike lignocellulosic precursors, the production of biochar through pyrolysis of sludge is limited due to its small surface area and amorphous nature. Marketable biochar from sludge, possessing decorated functional groups and enhanced surface area, is highly sought after.

Inspired by standard activated carbon production, biochar activated physically or chemically has gained broad interest thanks to its improved properties and effective utilization (Yu et al., 2020). Although physical activation unblocks the pores in carbon skeletons via partial oxidation of volatile carbon in biochar, a high content of inorganics in sludge commonly forming non-porous fractions restricts physical activation efficiency. Conversely, chemical activation utilizes the inorganic metallic chemicals (e.g., ZnCl_2 , KOH, etc.) to react with the carbon skeletons and create porous structures, possessing higher porosity development efficiency than physical activation. Redox reactions between carbon and KOH at high temperatures were mainly responsible for micropores development (Wang and Kaskel, 2012). Meanwhile, physical intercalation of ZnCl_2 could expand carbon lattices, and substantial mesopores were generated after the removal of these “metallic templates” by further washing (Huang et al., 2009). The mechanisms of chemical activation are variable depending on the reactivity of different activation agents and precursors. For instance, NaOH showed similar activation effects with KOH, but Na had an affinity for the carbon of lower structural order (Raymundo-Piñero et al., 2005). NaCl could also act as templates for porous carbon synthesis, but most pores developed were found to be nanopores instead of mesopores (Zhang et al., 2016). These alternative activation agents were rather less documented comparing with KOH/ ZnCl_2 , and their porosity development behaviors were not understood clearly.

Most metallic compounds with the potential of porosity development belonged to alkali and alkaline earth metals (AAEMs) species, which played crucial roles in the pyrolysis process of sludge. AAEMs in association with chlorides, carbonates, oxides and hydroxides can all catalyze the sludge pyrolysis process through secondary cracking of liquid products, thereby producing more char residuals. AAEM species in soluble or ion-exchangeable

form are more likely to vaporize during the pyrolysis process while those in the mineral phase tend to be fixed in the char residual. The vaporization of AAEM species is often associated with porosity development, and the remaining AAEM species could bind to the carbon skeleton implementing functionality on the material surface (Rawal et al., 2016). Although chemical activation using pure chemicals is often effective, a substantial amount of chemical dosing is needed, and the process generates secondary pollution. Hence, chemical activation with a low-cost source of AAEM species and reduced secondary pollution is crucial in turning sludge to quality biochar. Seawater containing large amounts of AAEM species such as sodium, magnesium, calcium, and potassium could act as a coagulant (Liu et al., 2011) to bridge various negatively charged functional groups (e.g., carboxyl groups), thereby generating metal organics in the sludge matrix and possibly enabling in situ catalysis for subsequent sludge pyrolysis. If catalytic pyrolysis could be achieved using minerals originating from seawater, then involving seawater in the sludge treatment system would naturally impregnate the sludge matrix with metallic catalysts for pyrolysis. Dewatered saline sewage sludge produced from seawater uses (e.g., seawater toilet flushing in Hong Kong, China) or infiltration/intrusion would become the most widely available precursor pre-impregnated with AAEM catalysts for modified biochar production.

Apart from material modification, exploring the application domain of sludge-derived biochar is also of interest. Biochar is no longer used only for the soil amendment or as a catalyst or adsorbent (Cha et al., 2016). Modified biochar with a large surface area is a promising candidate for electrochemical capacitor fabrication (Cheng et al., 2017). Energy storage mechanisms of biochar electrodes include electrochemical double-layer capacitance (EDLC) and pseudo-capacitance (PC), where the surface area and functional groups of biochar play a key role. Using sludge-derived biochar as capacitive carbon has been demonstrated feasible recently (Feng et al., 2015, Li et al., 2018), but the activation through KOH was inevitable. The motive of resource utilization of sewage sludge faces a contradiction among actual useful resource, costly recovery, and processing. In light of this, this study, therefore, examined the feasibility of using a “seawater-in-sludge” approach for capacitive biochar production from sewage sludge (Fig. 1). Freshwater sludge was mixed with seawater and dried as the precursor for biochar production. Characteristics of the produced biochar, including surface area, functional groups, and morphology were examined. Electrochemical tests (cyclic voltammetry, galvanostatic charge-discharge cycling, and electrochemical impedance spectroscopy) were conducted to test the capacitive behavior. The findings offer a cost-effective route for simultaneous sewage sludge disposal and functional biochar production.

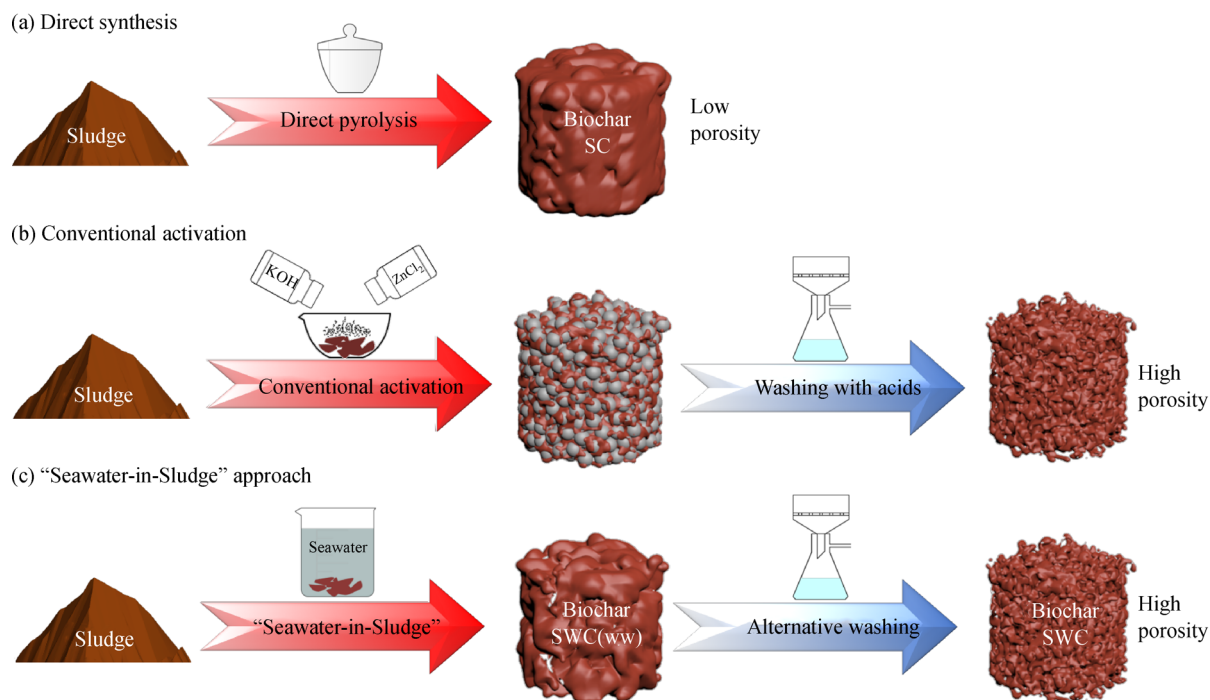


Fig. 1 Scheme illustration of biochar production from sewage sludge: (a) Direct synthesis by pyrolysis of sewage sludge; (b) Conventional chemical activation using KOH or ZnCl₂ with post-acids-washing for porosity development in biochar; (c) Environmental "Seawater-in-Sludge" approach with alternative washing for biochar modification.

2 Materials and methods

2.1 Source of Raw sludge

Raw sewage sludge was sampled from a local WWTP in Hong Kong. The sludge was washed with ultrapure water after sampling and then freeze-dried to retain as much of the organic fractions as possible. The dried sludge was crushed in a mortar and stored in the fridge at -20°C . Seawater after straining and electrochlorination was collected from the Hong Kong seawater toilet flushing network. Salinity at the point of collection was 3.2% with no residual free chlorine.

2.2 Synthesis of "seawater in sludge" biochar (SWC)

The impregnation of sludge particles with seawater was achieved by direct physical mixing. Three grams of dried sludge particles with a mean diameter of approximately 100 μm were soaked in seawater for 3 h at room temperature. The resulted slurry was mechanically dewatered and dried in an oven at 105°C . The pre-treated sludge was then stored in the dryer as feedstock for the pyrolysis step. The pyrolysis of the feedstock was conducted in a tubular furnace with constant nitrogen supply. The feedstock was heated in a quartz vessel from room temperature to the final temperature at a heating rate of $10^{\circ}\text{C}/\text{min}$ and kept at the final temperature for a residence time of 1 h. Three different final temperatures (600°C , 750°C , and

900°C) were examined to evaluate the effect of pyrolysis temperature on the carbon properties. The yield of biochar residual was estimated from $\text{yield (\%)} = \text{dry weight of char} \div \text{dry weight of precursor} \times 100$ before post-treatment. After pyrolysis, the biochar samples were washed with 6N hydrochloric acid (HCl) followed by deionized water and then dried in the oven at 105°C . Resulting samples were denoted by SWC-600, SWC-750 and SWC-900. Control groups not washed with acid were obtained for comparison and denoted by SWC (ww). Biochar derived from raw sludge and washed only with deionized water was referred to as SC-600, SC-750 and SC-900. Samples and synthesis conditions are summarized in Table 1.

The energy demand of "seawater in sludge" approach was estimated on the basis of 1 t/h thickened sludge with an initial solid concentration (S_{initial}) of 5% treated. Mechanical dewatering ($S_{\text{dewatered}} = 30\%$), followed by thermal drying ($S_{\text{dried}} = 90\%$) was considered in sequence. The energy required was 10 kWh/t water removed for mechanical dewatering and 800 kWh/t water removed for thermal drying, respectively (Mahmoud et al., 2011), and the energy recovery from pyrolysis reactor was considered as 3100 kWh/t dry mass treated (Mills et al., 2014).

2.3 Physiochemical analysis

Proximate and elemental analysis was conducted on dried sludge (Table S1) using an Elementar-Vario Macro Cube (Germany). Fourier transform infrared (FTIR) spectra

Table 1 Sample names and synthesis methods

| Sample names | Synthesis methods |
|--|--|
| SWC-600, SWC-750, SWC-900 | Seawater-impregnated sludge pyrolyzed at 600°C, 750°C, 900°C followed by washing with acids and deionized water. |
| SC-600, SC-750, SC-900 | Freshwater sludge directly pyrolyzed at 600°C, 750°C, 900°C followed by washing with acids and deionized water. |
| SWC-600 (ww), SWC-750 (ww), SWC-900 (ww) | Seawater-impregnated sludge pyrolyzed at 600°C, 750°C, 900°C followed by washing with deionized water only. |
| SC-600 (ww), SC-750 (ww), SC-900 (ww) | Freshwater sludge directly pyrolyzed at 600°C, 750°C, 900°C followed by washing with deionized water only. |

(500–4000 cm^{-1}) of raw sludge was collected with a Vertex 70 FTIR spectrometer (Hyperion 1000, Bruker). The surface areas and porosity distributions of SWC and SC were examined from nitrogen adsorption-desorption isotherms (Nova 3200e, Quantachrome Instruments). The surface areas were determined using the Brunauer-Emmett-Teller (BET) method. The porosity distributions were calculated by density functional theory (DFT). A scanning electron microscope (SEM, JSM6390, JEOL) was used to observe the morphology of biochar. A transmission electron microscope (TEM, JEM 2010F, JEOL) was used to examine the detailed texture of biochar. X-ray photoelectron spectroscopy (XPS) spectra were obtained from a Kratos Axis Ultra XPS system using an Al $K\alpha$ monochromatic source. The high-resolution spectra were deconvoluted using XPSPEAK 4.1 software under the scheme mentioned by Smith et al. (2016). The biochar samples were analyzed by a powder X-ray diffractometer (XRD) (SPW1830, Philips) with a ceramic tube scattering from 15° to 75°. Raman spectra were recorded using a Raman microscope (RAMANMICRO 300, Perkin Elmer). Thermogravimetric (TG) and differential thermogravimetric (DTG) tests of dried sludge were performed on a thermogravimetric analyzer (Q5000, TA instruments, USA). The incorporated minerals in the SWC precursor were quantified with an inductively coupled plasma-optical emission spectrometer (725 ES, VARIAN) after digestion.

2.4 Electrochemical testing

Nickel foil (1 cm^2) was coated with a slurry of 80% carbon materials, 10% carbon black (Super-P), and 10% polyvinylidene fluoride (PVDF) binder in N-methylpyrrolidone (NMP) and placed in the oven for drying at 105°C to form a working electrode. The capacitance of biochar was tested in a three-electrode configuration with 1M Na_2SO_4 as the electrolyte in an airtight three-electrode vessel. Pt wire was used as the counter electrode and Ag/AgCl was used as the reference electrode. Cyclic voltammetry (CV) and galvanostatic charge-discharge cycling (GCD) were performed using an electrochemical workstation (PMC-2000, PAR-STAT MC, Princeton Applied Research). The CV curves were obtained in the range of 0–0.8V vs. Ag/AgCl by

varying the scan rate from 5 to 200 mV/s. GCD tests were carried out with different current densities ranging from 0.5 to 8 A/g within the potential range of 0–0.8 V vs. Ag/AgCl. The specific capacitance calculated from the CV curves is expressed by Eq. (1),

$$C = \frac{\int_0^{2V_0} \frac{v}{v} |i| dt}{2mV_0} \quad (1)$$

where V_0 is the potential window, v is the scan rate, i is the current, and m is the mass value of SWC.

The current response to scan rate varies depending on whether the process is diffusion-controlled (PC) or surface controlled (EDLC). The contribution of pseudo-capacitance (PC) was quantified by Eq. (2) at different scan rates in CV tests (Liu et al., 1998).

$$\frac{i(v)}{v^{0.5}} = k_1 + k_2 v^{0.5} \quad (2)$$

where $i(v)$ is the current response, v is the scan rates, k_1 represents the contribution of diffusion current while k_2 represents the contribution of capacitive current. By linear regression of $i(v)$ and $v^{0.5}$ at different scan rates, one can estimate the value of k_1 and k_2 .

Electrochemical impedance spectroscopy (EIS) was also recorded using the same electrochemical workstation from 0.01 to 100000 Hz at the open-circuit voltage with an alternate current amplitude of 5 mV. The complex capacitance was calculated based on Eq. (3–5)

$$|Z| = \sqrt{\text{Re}(Z)^2 + \text{Im}(Z)^2} \quad (3)$$

$$\text{Re}(C) = \frac{-\text{Im}(Z)}{2\pi f |Z|^2} \quad (4)$$

$$\text{Im}(C) = \frac{\text{Re}(Z)}{2\pi f |Z|^2} \quad (5)$$

where $\text{Re}(C)$ and $\text{Im}(C)$ are real part and imaginary part of complex capacitance, $\text{Re}(Z)$ and $\text{Im}(Z)$ are real part and imaginary part of complex impedance, f is the frequency.

The capacitance (C) was also calculated by GCD tests

Eq. (6) and the respective energy and power densities were estimated by Eqs. (7) and (8).

$$C = \frac{I \times t}{m \times V_0} \quad (6)$$

$$E = \frac{\frac{1}{2} \times C \times V_0^2 \times 1000}{3600} \quad (7)$$

$$P = \frac{E \times 3600}{t} \quad (8)$$

where E represents energy density, P represents power density, V_0 represents the potential window, m is the mass of active material used for electrode fabrication, t is the discharging time during constant charge and discharge tests.

3 Results

3.1 Biochar yield

The “seawater-in-sludge” approach improved the biochar yield of slow pyrolysis (Fig. 2(a)). The SWC yield was about 10% higher than the SC yield. The highest biochar yield was 32.9% and occurred when the pyrolysis temperature was 600°C. Thermogravimetric analysis results (Fig. 2(b)) confirmed the higher yield of SWC and indicated that the weight loss mostly occurred from 200°C to 600°C. Decreased biochar yield of all samples was associated with increased pyrolysis temperature. The energy demand was estimated based on the reported values (Fig. S6). The net power requirement was estimated to be 39.26 kW with the assumption of 1 t/h sludge mixed liquid treated. A large proportion (80%) of the dewatering energy requirement could be offset by the pyrolysis process if the

volatile compounds were used for energy production (Mills et al., 2014).

3.2 Biochar texture

Morphology of biochar was examined using an SEM and a TEM. As observed in low-resolution SEM images, SWC showed a rough, angular structure (Figs. 3(a)–3(b)) while SC exhibited a relatively smooth “hill-like” structure (Fig. S2(a)–S2(b)). This difference was likely caused by the volatilization of unpyrolysed carbon and ash content with the activation of AAEM ions. Pores observed with a TEM were mostly mesopores (Fig. 3(c)) and micropores (Fig. 3(d)). Abundant mineral crystals were also found in the unwashed biochar samples (Fig. S2(c)). The crystals trapped in the carbon framework likely resulted from unreacted mineral ions during pyrolysis. With further washing, the trapped crystals were removed which resulted in a higher porosity.

3.3 Surface area and porosity distribution

The “seawater-in-sludge” synthesis resulted in biochar with a larger surface area (Table 2). The nitrogen physisorption isotherms of all samples (Fig. 3(e)) coincided with type IV isotherms according to IUPAC’s classification, indicating that the biochar obtained was likely a mesoporous material. The hysteresis loops followed type H4 loops, implying the presence of both micropores and mesopores (Thommes et al., 2015). Porosity distribution (Fig. 3(f)) calculated by DFT confirmed the presence of both micropores and mesopores. Physical mixing with seawater did not lead to a significant increase in the surface area of SWC at a pyrolysis temperature of 600°C. However, at higher pyrolysis temperatures, the effect of seawater impregnation became non-negligible. A higher pyrolysis temperature was associated with an increased biochar surface area which

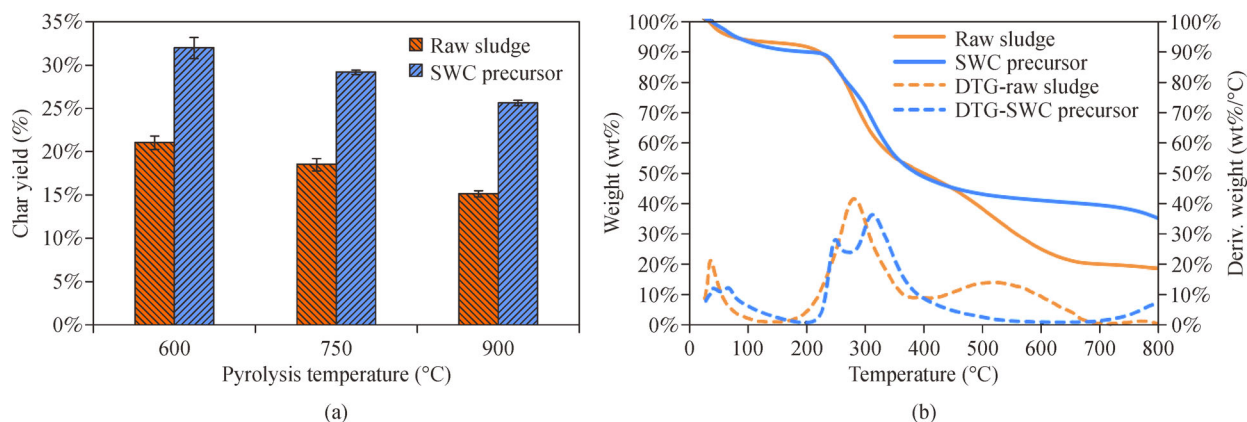


Fig. 2 (a) Biochar yield under different pyrolysis temperatures (i.e., 600°C, 750°C, 900°C); and (b) thermogravimetric analysis (TGA) of raw sludge and SWC precursors at 10°C/min.

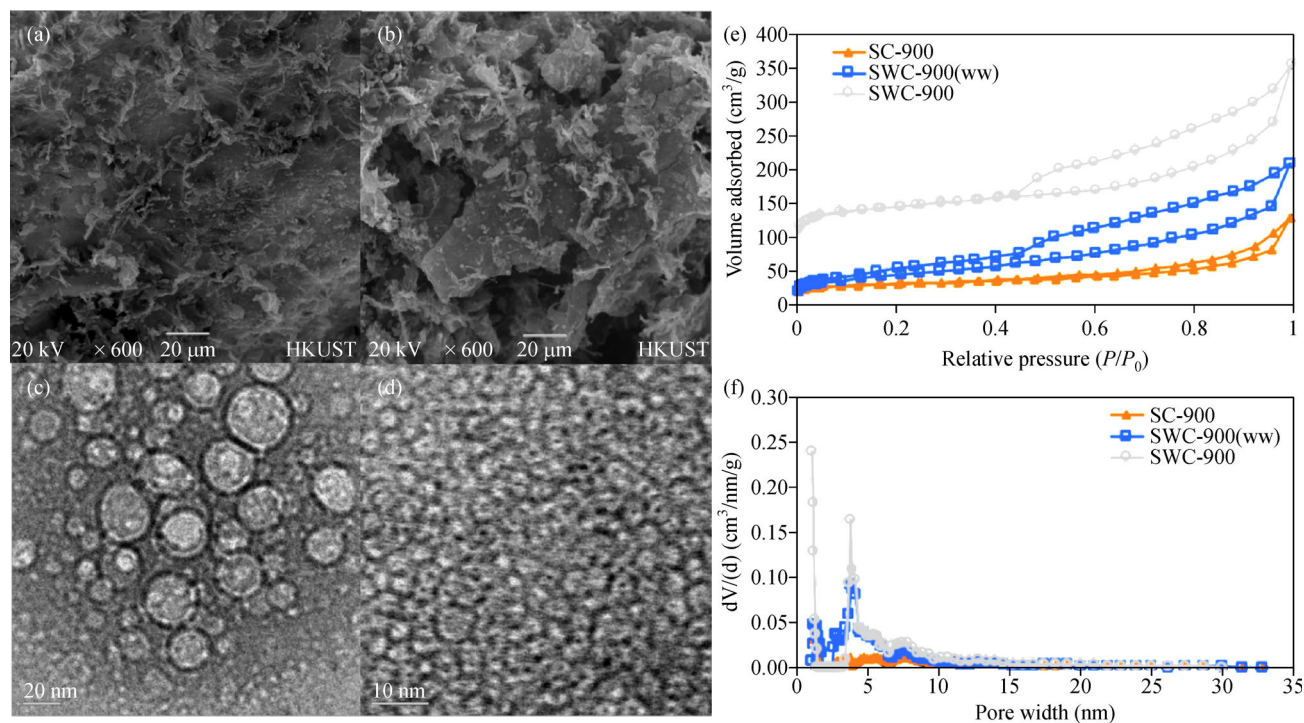


Fig. 3 (a–b) SEM images of surface morphology of SWC-900; and (c–d) TEM images of mesopores and micropores in SWC-900. (e) Nitrogen sorption isotherms of different carbon composites; and (f) Porosity distribution of different carbon composites calculated by density functional theory.

Table 2 BET surface area and pore volumes of different biochar samples

| Sample | S_{BET} (m ² /g) | $V_{\text{total pore}}$ (cm ³ /g) | V_{micro} (cm ³ /g) | V_{meso} (cm ³ /g) | $V_{\text{micro}}/V_{\text{total pore}}$ |
|--------------|--------------------------------------|--|---|--|--|
| SC-600 | 16.3 | 0.05 | N.A. | 0.05 | N.A. |
| SC-750 | 24 | 0.045 | 0.0028 | 0.0422 | 6.2% |
| SC-900 | 99.8 | 0.153 | N.A. | 0.153 | N.A. |
| SWC-600 | 153.1 | 0.305 | 0.0229 | 0.2821 | 7.5% |
| SWC-750 | 480.3 | 0.527 | 0.1175 | 0.4095 | 22.3% |
| SWC-900 | 457 | 0.462 | 0.1565 | 0.3055 | 33.9% |
| SWC-600 (ww) | 24.1 | 0.049 | N.A. | 0.049 | N.A. |
| SWC-750 (ww) | 103.3 | 0.115 | 0.031 | 0.084 | 27.0% |
| SWC-900 (ww) | 159.3 | 0.283 | 0.0243 | 0.2587 | 8.6% |

might be attributed to that the temperature was high enough to trigger catalytic reactions between minerals and carbon atoms. To further boost the surface area of sludge-derived carbon composites, acid washing was essential. The surface area reached 480.3 m²/g for SWC-750.

3.4 Surface chemistry of biochar samples

Two characteristic peaks at 1365 cm⁻¹ and 1590 cm⁻¹ of biochar samples were depicted by Raman spectra (Figs. 4(a) and 4(b)) which are the D (defect) band and the G (graphitic) band, respectively. The D band reflects the disorder degree, while the G band reflects the graphitiza-

tion degree of carbon materials. The intensity ratio I_G/I_D of SWC (1.12) was higher than that of SC (1.01), especially at a high pyrolysis temperature (i.e., 900°C), implying a higher graphitization degree was achieved when the feedstock contained seawater. Also, the I_G/I_D ratio increased with pyrolysis temperature with the G band becoming sharper. No clear G band was observed when sewage sludge was directly pyrolyzed at 600°C. XRD spectra (Fig. 4(c)) confirmed the higher graphitization degree of SWC with a higher empirical parameter (R). The inset illustrated the calculation procedure of R, namely the ratio of graphite peak intensity to background intensity. It has been suggested that R-value increases as the

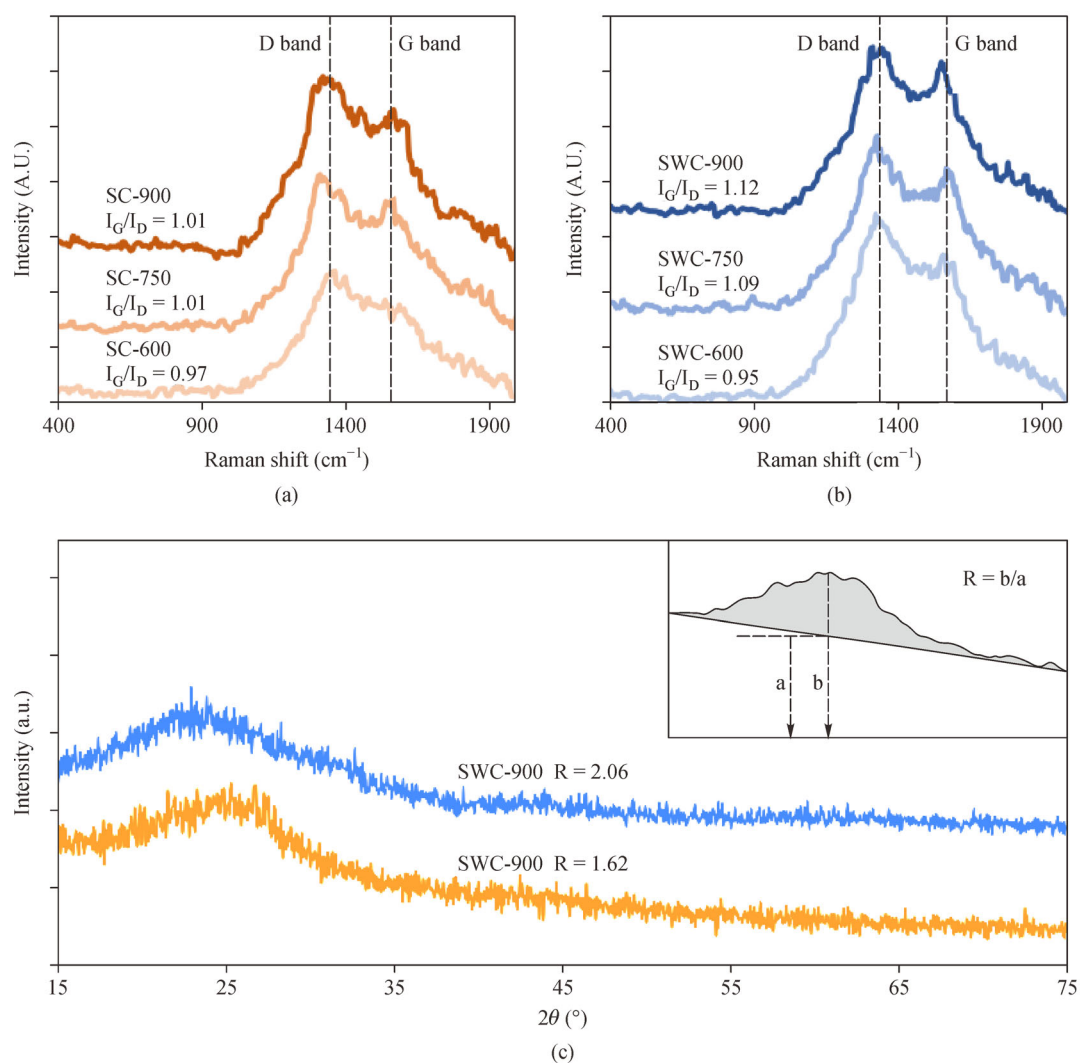


Fig. 4 (a) Raman spectra of biochar derived from direct pyrolysis of sewage sludge at different temperatures; and (b) Raman spectra of biochar derived from pyrolysis of sewage sludge impregnated with seawater. (c) XRD spectra of SWC-900 and SC-900 with calculated empirical factor (R).

concentration of parallel single layers increases, indicating a positive correlation between R -value and graphitization degree (Liu et al., 1996).

XPS survey spectra displayed three typical peaks corresponding to C 1s, N 1s and O 1s showing that carbon, nitrogen and oxygen are the dominant elements in biochar surfaces (Fig. S3). SWC-900 had a higher carbon concentration and lower nitrogen and oxygen concentrations than SC-900. Mass concentration (Table S2) of most heteroatoms except phosphorus decreased in SWC-900. The catalytic effect of seawater minerals during sludge pyrolysis removed a portion of the nitrogen and oxygen functional groups in the final product. XPS results suggested that besides volatilization and catalysis during pyrolysis, NaCl was also incorporated into the biochar samples. Abundant sodium and chlorine species were

found in the control group of SWC without washing. Sodium found in ICP analysis of biochar and mineral composites observed with the SEM is consistent with this finding.

The chemical state of major elements on biochar surfaces was explored by a high-resolution XPS scan (Fig. 5). Quantification of individual peaks (Tables S3–S5) showed that the relative weight of C–C/C = C in SWC-900 was higher than that in SC-900. C 1s spectra showed a tail between 286 eV and 293 eV which could be assigned to C–O (286 eV), C = O (287.5 eV), O = C–O (289 eV) and Pi-pi* (293 eV). Fewer oxygen groups were embedded in the carbon matrix after catalytic pyrolysis. The suppression of oxygen-containing groups by activation of immobilized minerals was also found by Zhu et al. (2011). N 1s spectra were deconvoluted to four peaks representing pyridinic-N

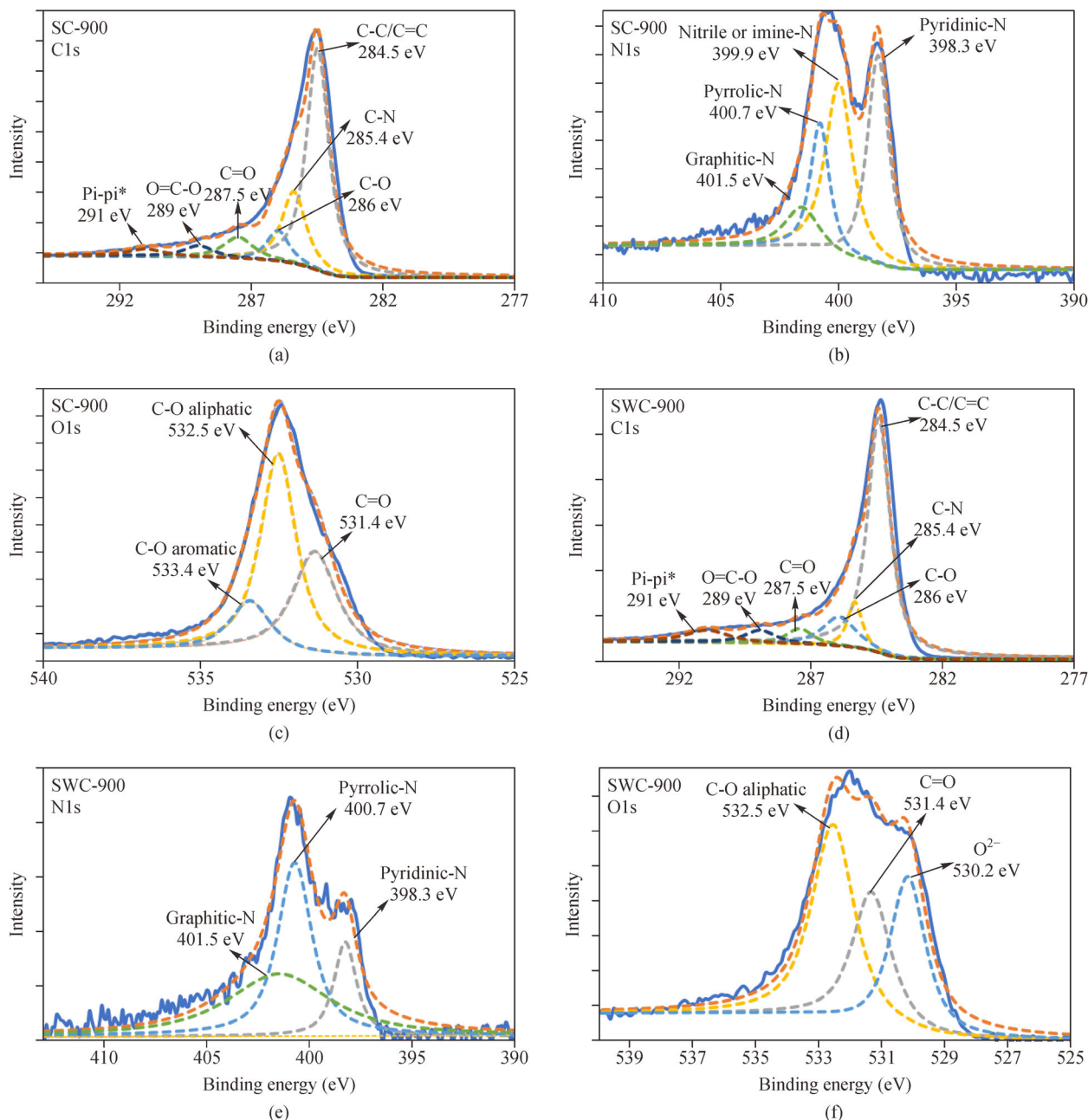


Fig. 5 High-resolution XPS scan of SC-900 and SWC-900: (a) C 1s of SC-900; (b) N 1s of SC-900; (c) O 1s of SC-900; (d) C 1s of SWC-900; (e) N 1s of SWC-900; and (f) O 1s of SWC-900.

(398.3 eV), nitrile or imine-N (399.9 eV), pyrrolic-N (400.7 eV) and pyridinic-N (401.5 eV). After activation by minerals, the relative weight of pyridinic-N and nitrile or imine-N decreased significantly. Graphitic-N became dominant in nitrogen functional groups. More graphitic groups were found in SWC than in SC which is consistent with Raman analysis. In terms of O 1s spectra, a different peak was identified as O^{2-} at 530.2 eV in SWC. The O^{2-} peak likely originated from oxide species during the formation of SWC.

3.5 Electrochemical performance

To examine the potential of using SWC as an electrodes material, both SC-900 and SWC-900 were assembled in a three-electrode system and characterized via CV and GCD tests. Despite the presence of N and O heteroatoms in SWC and SC, no obvious hump peaks were observed during CV tests, suggesting the contribution of pseudo-capacitance was not significant. The rectangular and symmetric shapes of CV curves, along with the triangular GCD curves

indicated the capacitance was a result of EDLC (Fig. 6(a)). The contribution of PC was quantified to be less than 20% in SWC-900 (Fig. S5(a)) while its contribution in SC-900 is higher (Fig. S5) due to more N and O heteroatoms. SWC-900 showed a larger loop in the CV curve (Fig. 6(a)) than SC-900 suggesting it had a higher capacitance. The highest specific capacitance found in the CV tests was 113.9 F/g for SWC-900 calculated at 5 mV/s. The CV curves became distorted and the specific capacitance decreased with increased scan rate (Figs. 6(c) and 6(d)). The specific capacitance dropped sharply at low scan rates and became stable at high scan rates. This phenomenon was observed in all tests due to insufficient time for ion diffusion and transport through the material pores at high scan rates (Conway, 2013). Similar trends were observed when the current density was increased in the GCD tests (Fig. 6(e)). The capacitance retentions of SC-900 and SWC-900 were 24% and 41%, respectively. SWC-900 showed better capacitive performance at high scan rates. The ohmic drop (IR drop) of SWC-900 was slightly lower than that of SC-900 at 0.5 A/g, implying a lower internal resistance of SWC-900 (Fig. 6(b)). The capacitance retention was 93% after 10000 cycles (Fig. 6(f)) with the CV curves remaining quasi-rectangular and symmetric. The excellent durability and stability of SWC-900 also made it a promising candidate for supercapacitor fabrication.

EIS tests were further conducted to characterize the

capacitive behavior of both SC-900 and SWC-900. Nyquist plot (Fig. 7(a)) showed an approximately straight line in the low-frequency region and a semicircle in the high frequency region. The spectra of SWC-900 was more vertical than SC-900 indicating higher capacitance of SWC-900. The vertical impedance data reflected ideal capacitive behavior in the low frequency region and the semicircle in the high-frequency region was an indication of charge-transfer resistance. The resistance is correlated with the diameter of the semicircle. To validate the charge-transfer resistance, an equivalent circuit was constructed and fitted with EIS spectra data. The components include R_s , the solution resistance between the reference electrode and the working electrode; R_{ict} , the interfacial charge-transfer resistance between electrode and electrolyte; Z_w , the Warburg impedance; C_{dlc} , capacitance resulted from EDLC, C_p , capacitance resulted from PC. The R_s and R_{ict} were calculated to be 0.91 Ω and 0.39 Ω for SWC-900 while 1.26 Ω and 0.76 Ω for SC-900, respectively. The lower resistance of SWC-900 allowed faster ion transport through the porous network than SC-900 which favored its usage as capacitive material. The Bode plots (Fig. 7(c)) confirmed the superior capacitance of SWC-900 with a relaxation maximum of $Im(C)$ observed at 0.25Hz ($\gamma_0 = 3.98s$). The relaxation time (γ_0) is an indication of how long the capacitor takes to reach 50% of its maximum capacitance at low frequency. A shorter relaxation time indicates better charge/discharge reversibility and effi-

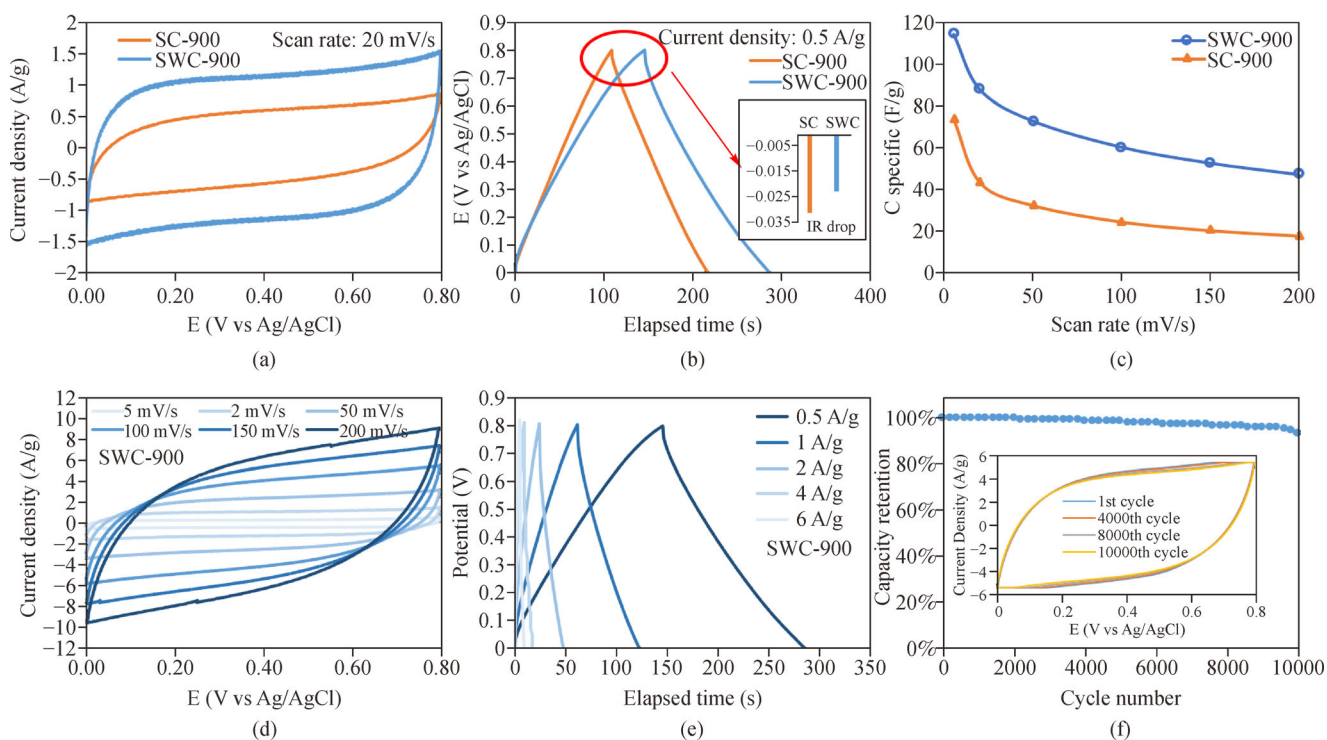


Fig. 6 (a) Cyclic voltammetry (CV) tests of SC-900 and SWC-900 at 20 mV/s. (b) Galvanostatic charge/discharge (GCD) curves. The inset in (b) shows the IR drops. (c) Specific capacitance of SWC-900 at different scan rates in CV tests. (d) CV of SWC-900 at different scan rates. (e) GCD of SWC-900 at different current densities. (f) Long-term durability test of SWC-900.

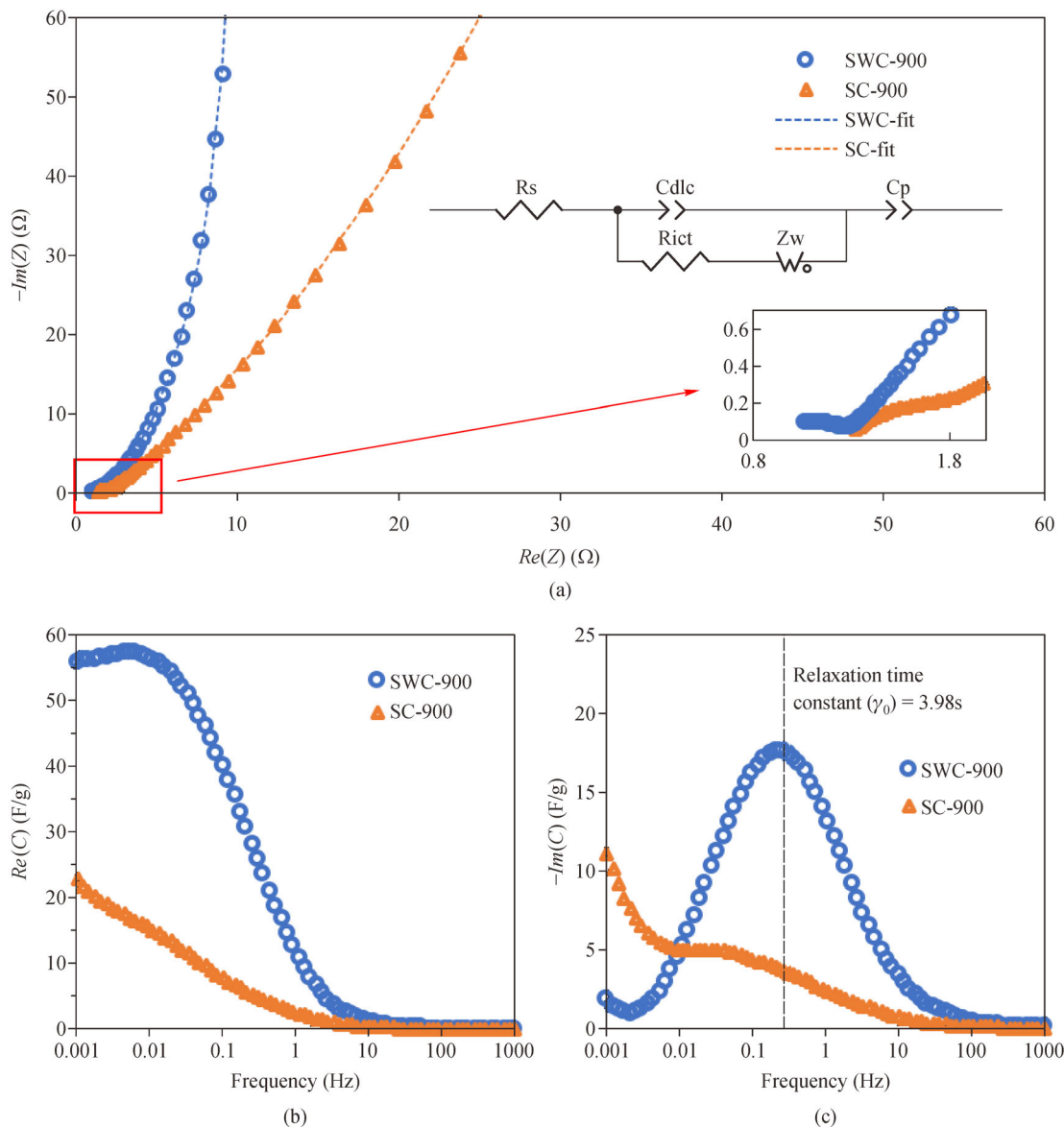


Fig. 7 (a) Nyquist plots of SC-900 and SWC-900. The inset in (a) is the equivalent circuit and the magnified plot in the higher frequency region. (b) Bode plots of SC-900 and SWC-900, the frequency dependence of real capacitance $Re(C)$. (c) Bode plot, the frequency dependence of imaginary capacitance $Im(C)$.

ciency which is also known as the supercapacitor factor of merit (Miller, 1998).

4 Discussion

4.1 Effect of NaCl on porosity development during pyrolysis

A higher surface area was obtained in SWC than in SC in this study. Sodium was the dominant species found in precursors and biochar samples (Table 2) so presumably it was the functional species. The concentration of sodium (typically around 10 g/L) was at least one order of

magnitude higher than that of other cations in natural seawater which explained the enormous amount of sodium species in sludge after mixing with seawater. It is well accepted that NaCl loading during pyrolysis improves char yield (Jakab et al., 1997) while pore development in char residuals by NaCl activation remains contested. NaCl is believed to block the pores inside the biochar structure under mild pyrolysis temperatures (Sizmur et al., 2017). Conversely, Quyn et al. (2002) observed sodium volatilization from 600°C, and Okeola et al. (2012) obtained samples with a higher surface area when NaCl was added as an activation agent. In this study, biochar samples with larger surface areas were obtained at all pyrolysis temperatures when sludge was pre-impregnated with

seawater. To eliminate the effect of washing on pore development, a control experiment without washing was also conducted (Fig. 2(a)). A larger surface area was still observed for SWC without washing. Associated with the metal analysis (Table S6), NaCl volatilization might have contributed to the increased surface area to a certain degree in this study. The volatilization of Na was found to be independent of Cl volatilization during pyrolysis (Quyn et al., 2002). According to this finding, Na and Cl did not volatilize as NaCl molecule but Cl was volatilized prior to Na leaving the Na as-COONa into the char matrix instead. Later, the Na was volatilized with carboxylate groups causing a decrease in oxygen functional groups and an increase in porosity. This hypothesis is applicable in this study where fewer oxygen functional groups were observed in SWC by XPS and sodium volatilization was observed by ICP analysis. Carboxyl groups identified in the IR spectrum (Fig. S1) of raw sludge also supported the presence of-COONa.

Other than sodium, potassium, calcium, and magnesium levels in both SC and SWC decreased with elevated pyrolysis temperature while aluminum, iron and copper levels increased in biochar after pyrolysis. Volatilization of light metal species and concentration of heavy metal species during sludge pyrolysis was verified in this study. However, abundant NaCl was still observed by ICP and XPS (Fig. S4) in SWC without acid washing suggesting NaCl was only partially volatilized. Considering the crystals trapped in the carbon framework (Fig. S2(c)), other mechanisms might have contributed to the porosity development.

4.2 Molten-salt effect on porosity development during pyrolysis

Molten salt has been reported to facilitate porosity development if miscibility can be maintained between the salt melt and the carbonizing material during pyrolysis. The dehydration reaction likely occurred before the salt melt temperature was reached, thereby creating voids for the fluid molten salt to transfer heat and mass (Yin et al., 2014). Then molten salt percolation occurred inside the carbon structure at elevated temperatures, resulting in a pore size similar to that in the salt structures. The salt phase could be easily removed from carbon structures by further washing. In this study, the molten-salt effect likely contributed to the increased surface area of SWC at high pyrolysis temperatures (i.e., 750°C and 900°C). However, the melting point of NaCl is 801°C which is higher than the pyrolysis temperature of 750°C. First, the vaporization of Na was observed suggesting that some of the sodium in the feedstock might exist as-COONa, which has a much lower melting point than NaCl molecules. Second, a multi-salt system tends to lower the melting point compared with an individual salt component due to the presence of the eutectic system (Ambrosek, 2011). Abundant magnesium,

calcium and potassium were also found in the SWC precursor. The melting point of molten salt in this study could be lower than that of single NaCl.

Herein, we proposed the synergistic mechanism including both mineral volatilization and molten-salt effect for “seawater-in-sludge” activation (Fig. 8). The sequence of melting and volatilization depended on the physical properties of specific mineral species and their interaction. Taking NaCl for example, the prior volatilization of Cl in NaCl allowed the formation of-COONa whose melting in turn facilitated heat and mass transfer, thereby distributing the available energy for more minerals to volatilize. These two mechanisms created a positive feedback loop for porosity development (activation). After activation, a final acid washing eliminated the mineral species and open pores previously occupied by mineral crystals to further boost the surface area.

4.3 Role of biochar properties in the capacitance of biochar-derived supercapacitors

The performance of capacitors fabricated from biochar is closely related to the latter’s chemical and physical properties such as conductivity, surface area, and pore structures. In this study, SWC-900 presented a lower internal resistance (smaller IR drop and semicircle diameter) than SC-900 during GCD and EIS tests. The resistance of the current-carrying path (also known as intra-particle resistance) is determined by the chemical and structural morphology of carbon particles.

Another possible contributing factor to resistivity could be oxygen functionalities which preferentially formed at the edges of the graphite-like structure, raising the barrier to electron transfer (Polovina et al., 1997). XPS detected more oxygen functional groups in SC-900 than in SWC-900 which might also explain the former’s higher internal resistance.

Specific capacitance (F/g) is usually proportional to the surface area since the EDLC stores energy at the interface between electrode and electrolyte. However, in practice, the surface area measured by nitrogen adsorption might not be representative of that accessible to the electrolyte. Table S7 summarized performances of biomass-derived carbon electrodes for supercapacitor fabrication. SWC-900 obtained in this study presented a smaller surface area than other carbon materials with activation of KOH (Peng et al., 2018) but its specific capacitance per area (24.9 uF/cm²) is higher. This might be attributed to the optimal pore size distribution of SWC-900. As calculated by DFT theory, the pore size in SWC-900 mostly ranged from 1 nm to 30 nm and the micropore volume accounted for over 30% of the total pore volume. A hierarchical structure containing both micropores and mesopores has long been demonstrated to be ideal for energy storage as mesopores provide fast ion-transportation channels while micropores offer the main ion storage sites (Su et al., 2011). The

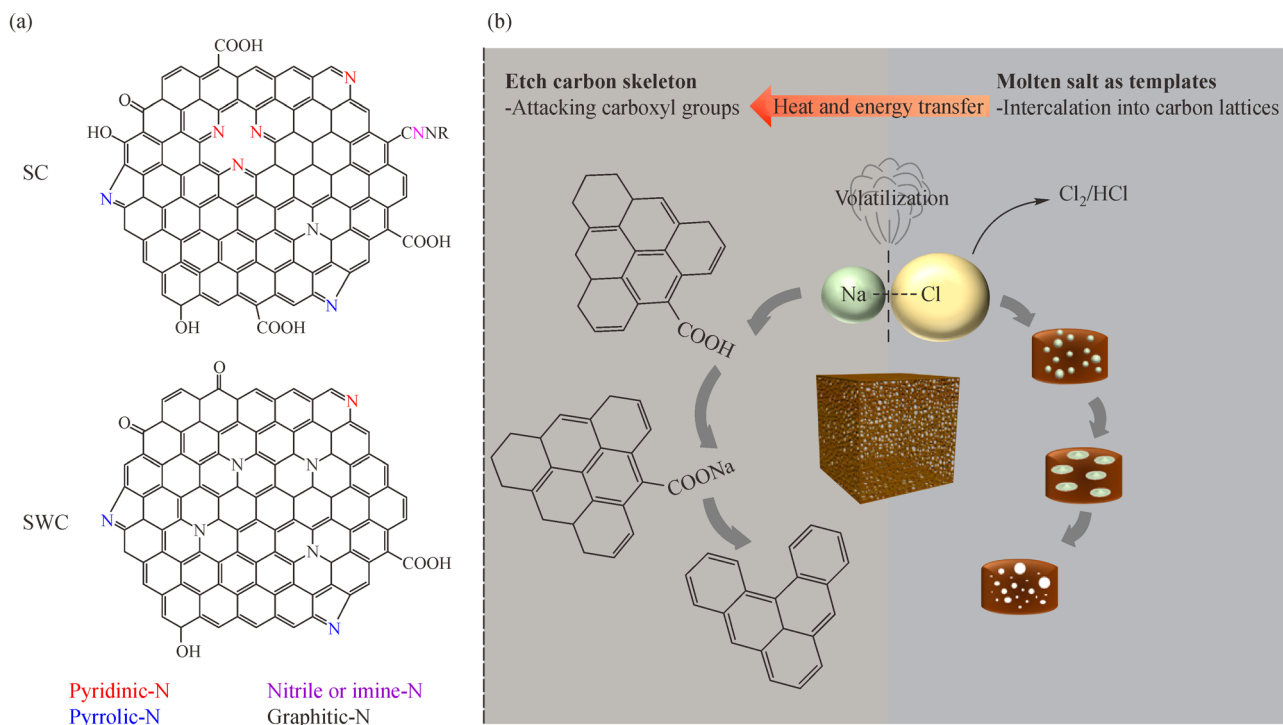


Fig. 8 (a) Illustration of functional groups in carbon lattice: SC with more oxygen functional groups and pyridinic-N, nitrile or imine-N groups; SWC with less oxygen functional groups and graphitic-N became dominant nitrogen functional groups. (b) Proposed synergetic mechanisms for “Seawater-in-Sludge” approach: NaCl melted as templates for mesopores development meanwhile acting as heat and energy transfer medium for the volatilization of NaCl. Na and Cl didn’t volatilize as NaCl molecule while Cl volatilized prior to Na leaving Na as an etching agent to attack oxygen functional groups creating porosity.

greater percentage of micropores in SWC-900 contributed to its superior capacitive behavior.

4.4 Possible limitations

Possible limitations of this study might result from the abundant anionic chloride introduced by seawater along with the AAEM cations. The chloride release is temperature dependent and mainly released as HCl(g) at low temperature region, and partially released as gaseous organic chloride compounds, Cl₂(g) or metal chlorides sublimation at high temperature region. The species of volatile chloride compounds also varied with different organic precursors and metal additives. In this study, based on the TGA analysis, most chloride compounds volatilized as HCl(g). Despite the minimum likelihood of NaCl sublimation regarding its high boiling point, the Cl might be captured by other metallic species such as K to form KCl whose sublimation was observed after 800°C (Wang et al., 2010). Organic chloride compounds emission is a challenging issue for most thermochemical processes due to the potential presence of toxic compounds such as polychlorinated dibenzo-p-dioxins and dibenzofurans (PCDD/Fs). PCDD/Fs mostly formed during pyrolysis through a catalysis-assisted heterogenous pathway with a temperature window of 200°C–400°C due to the absence of

oxygen (Altarawneh et al., 2009). It has been reported alkaline earth metal could suppress the formation of PCDD/Fs (Qian et al., 2005). Considering the high concentrations of alkaline earth metals in the seawater, the formation of PCDD/Fs should be suppressed during pyrolysis of seawater-impregnated sludge in this study. Nevertheless, to confirm the fate of chloride species during pyrolysis further analysis is needed on the specific case. Agglomeration and/or slagging issue induced by AAEM species could be another limitation, as it is a common phenomenon of pyrolysis process dealing with high ash feedstocks. Volatile metallic compounds might condense at a lower temperature zone and cause sintering and fouling. This can be addressed by increasing the pyrolysis temperature and uniforming the heat distribution (Schmidt and Kaminsky, 2001). Comparing with the conventional activation methods which require 1-2 folds more chemical activation agents than precursor by mass, the usage of seawater is more environmentally-friendly in terms of the overall adverse impact.

4.5 Environmental implication

In this proof-of-concept study, seawater was found to benefit the porous biochar production from sewage sludge. Considering the large quantity of sewage sludge produced

and its high moisture content, the conventional KOH/ZnCl₂ activation strategy would be wasteful and not environmentally friendly. Involving seawater in the sludge treatment system could simultaneously improve sludge dewaterability and load AAEM catalysts into the sludge matrix. Future research is expected on exploring the interaction between sludge polymers and AAEM cations in the mixing stage. The findings of this study open a new path for sewage sludge treatment and resource recovery in coastal areas.

5 Conclusions

Inspired by catalytic pyrolysis using AAEM species for functional materials production, a “seawater-in-sludge” approach is developed to grow the activated biochar. The resulted biochar achieved boosted surface area and electrochemical capacitance. Seawater was proven to be an effective activation agent and the maximum surface area (480.3 m²/g) of SWC was obtained at pyrolysis temperature of 750°C. Higher graphitization degree and less functional groups were found in activated biochar resulting in lower electrical resistivity of SWC than SC. Acid washing is still essential to boost the surface area of the derived biochar for application as a capacitive material. The specific capacitance of SWC-900 was 113.9 F/g with good cyclic stability. AAEM vaporization and molten-salt templating were proposed to constitute the activation mechanism synergistically.

Acknowledgements This research was supported by the National Natural Science Foundation of China (Grant No. 51778165), Key Program of National Natural Science of China (Grant No. 51638005), Science and Technology Development Fund, Macao Special Administrative Region, China (File No. FDCT-0104/2018/A3, FDCT-0057/2019/A1), Start-up Research Grant of University of Macao (Grant No. SRG2018-00110-FST), the Research Grants Council of the Hong Kong Special Administrative Region, China (Project No. [T21-604/19-R]).

Electronic Supplementary Material Supplementary material is available in the online version of this article at <https://doi.org/10.1007/s11783-020-1295-0> and is accessible for authorized users.

References

- Altarawneh M, Długogorski B Z, Kennedy E M, Mackie J C (2009). Mechanisms for formation, chlorination, dechlorination and destruction of polychlorinated dibenzo-*p*-dioxins and dibenzofurans (PCDD/Fs). *Progress in Energy and Combustion Science*, 35(3): 245–274
- Ambrosek J W (2011). Molten chloride salts for heat transfer in nuclear systems. Dissertation for the Doctoral Degree. Madison: The University of Wisconsin- Madison
- Cao Y, Pawłowski A (2012). Sewage sludge-to-energy approaches based on anaerobic digestion and pyrolysis: Brief overview and energy efficiency assessment. *Renewable & Sustainable Energy Reviews*, 16(3): 1657–1665
- Cha J S, Park S H, Jung S C, Ryu C, Jeon J K, Shin M C, Park Y K (2016). Production and utilization of biochar: A review. *Journal of Industrial and Engineering Chemistry*, 40: 1–15
- Cheng B H, Zeng R J, Jiang H (2017). Recent developments of post-modification of biochar for electrochemical energy storage. *Bioresource Technology*, 246: 224–233
- Conway B E (2013). *Electrochemical supercapacitors: scientific fundamentals and technological applications*. New York: Springer Science & Business Media
- Feng H, Zheng M, Dong H, Xiao Y, Hu H, Sun Z, Long C, Cai Y, Zhao X, Zhang H, Lei B, Liu Y (2015). Three-dimensional honeycomb-like hierarchically structured carbon for high-performance supercapacitors derived from high-ash-content sewage sludge. *Journal of Materials Chemistry. A, Materials for Energy and Sustainability*, 3(29): 15225–15234
- Huang Y, Hu S, Zuo S, Xu Z, Han C, Shen J (2009). Mesoporous carbon materials prepared from carbohydrates with a metal chloride template. *Journal of Materials Chemistry*, 19(41): 7759–7764
- Jakab E, Faix O, Till F (1997). Thermal decomposition of milled wood lignins studied by thermogravimetry/mass spectrometry. *Journal of Analytical and Applied Pyrolysis*, 40–41: 171–186
- Lee J W, Hawkins B, Day D M, Reicosky D C (2010). Sustainability: the capacity of smokeless biomass pyrolysis for energy production, global carbon capture and sequestration. *Energy & Environmental Science*, 3(11): 1695–1705
- Li X, Wang Z, Guo L, Han D, Li B, Gong Z (2018). Manganese oxide/hierarchical porous carbon nanocomposite from oily sludge for high-performance asymmetric supercapacitors. *Electrochimica Acta*, 265: 71–77
- Liu J, Zhao G, Duan C, Xu Y, Zhao J, Deng T, Qian G (2011). Effective improvement of activated sludge dewaterability conditioning with seawater and brine. *Chemical Engineering Journal*, 168(3): 1112–1119
- Liu T C, Pell W G, Conway B E, Roberson S L (1998). Behavior of molybdenum nitrides as materials for electrochemical capacitors: Comparison with ruthenium oxide. *Journal of the Electrochemical Society*, 145(6): 1882–1888
- Liu Y, Xue J S, Zheng T, Dahn J R (1996). Mechanism of lithium insertion in hard carbons prepared by pyrolysis of epoxy resins. *Carbon*, 34(2): 193–200
- Mahmoud A, Arlabosse P, Fernandez A (2011). Application of a thermally assisted mechanical dewatering process to biomass. *Biomass and Bioenergy*, 35(1): 288–297
- Miller J (1998). *Proceedings of the 8th International Seminar on Double-Layer Capacitors and Similar Energy Storage Devices*, Deerfield Beach, FL, Dec 7–9
- Mills N, Pearce P, Farrow J, Thorpe R B, Kirkby N F (2014). Environmental & economic life cycle assessment of current & future sewage sludge to energy technologies. *Waste Management (New York, N.Y.)*, 34(1): 185–195
- Okeola O F, Odebummi E O, Ameen O M (2012). Comparison of sorption capacity and surface area of activated carbon prepared from *Jatropha curcas* fruit pericarp and seed coat. *Bulletin of the Chemical Society of Ethiopia*, 26(2): 171–180

- Peng L, Liang Y, Dong H, Hu H, Zhao X, Cai Y, Xiao Y, Liu Y, Zheng M (2018). Super-hierarchical porous carbons derived from mixed biomass wastes by a stepwise removal strategy for high-performance supercapacitors. *Journal of Power Sources*, 377: 151–160
- Polovina M, Babić B, Kaluderović B, Dekanski A (1997). Surface characterization of oxidized activated carbon cloth. *Carbon*, 35(8): 1047–1052
- Qian Y, Zheng M, Liu W, Ma X, Zhang B (2005). Influence of metal oxides on PCDD/Fs formation from pentachlorophenol. *Chemosphere*, 60(7): 951–958
- Quyn DM, Wu H W, Bhattacharya S P, Li C Z (2002). Volatilisation and catalytic effects of alkali and alkaline earth metallic species during the pyrolysis and gasification of Victorian brown coal: Part II. Effects of chemical form and valence. *Fuel*, 81(2): 151–158
- Rawal A, Joseph S D, Hook J M, Chia C H, Munroe P R, Donne S, Lin Y, Phelan D, Mitchell D R G, Pace B, Horvat J, Webber J B W (2016). Mineral–biochar composites: Molecular structure and porosity. *Environmental Science & Technology*, 50(14): 7706–7714
- Raymundo-Piñero E, Azaïs P, Cacciaguerra T, Cazorla-Amorós D, Linares-Solano A, Béguin F (2005). KOH and NaOH activation mechanisms of multiwalled carbon nanotubes with different structural organisation. *Carbon*, 43(4): 786–795
- Schmidt H, Kaminsky W (2001). Pyrolysis of oil sludge in a fluidised bed reactor. *Chemosphere*, 45(3): 285–290
- Sizmur T, Fresno T, Akgül G, Frost H, Moreno-Jiménez E (2017). Biochar modification to enhance sorption of inorganics from water. *Bioresource Technology*, 246: 34–47
- Smith M, Scudiero L, Espinal J, McEwen J S, Garcia-Perez M (2016). Improving the deconvolution and interpretation of XPS spectra from chars by ab initio calculations. *Carbon*, 110: 155–171
- Su F, Poh C K, Chen J S, Xu G, Wang D, Li Q, Lin J, Lou X W (2011). Nitrogen-containing microporous carbon nanospheres with improved capacitive properties. *Energy & Environmental Science*, 4(3): 717–724
- Thommes M, Kaneko K, Neimark A V, Olivier J P, Rodriguez-Reinoso F, Rouquerol J, Sing K S (2015). Physisorption of gases, with special reference to the evaluation of surface area and pore size distribution (IUPAC Technical Report). *Pure and Applied Chemistry*, 87(9–10): 1051–1069
- Wang J, Kaskel S (2012). KOH activation of carbon-based materials for energy storage. *Journal of Materials Chemistry*, 22(45): 23710–23725
- Wang X, Si J, Tan H, Ma L, Pourkashanian M, Xu T (2010). Nitrogen, sulfur, and chlorine transformations during the pyrolysis of straw. Presented at the Energy and Fuels, 5215–5221
- Yin H, Lu B, Xu Y, Tang D, Mao X, Xiao W, Wang D, Alshwabkeh A N (2014). Harvesting capacitive carbon by carbonization of waste biomass in molten salts. *Environmental Science & Technology*, 48(14): 8101–8108
- Yu J, Xu J, Li Z, He W, Huang J, Xu J, Li G (2020). Upgrading pyrolytic carbon-blacks (CBp) from end-of-life tires: Characteristics and modification methodologies. *Frontiers of Environmental Science & Engineering*, 1(2): 19
- Zhang Y, Huang L, Jiang W, Zhang X, Chen Y, Wei Z, Wan L, Hu J (2016). Sodium chloride-assisted green synthesis of a 3D Fe–N–C hybrid as a highly active electrocatalyst for the oxygen reduction reaction. *Journal of Materials Chemistry. A, Materials for Energy and Sustainability*, 4(20): 7781–7787
- Zhu Y, Murali S, Stoller M D, Ganesh K J, Cai W, Ferreira P J, Pirkle A, Wallace R M, Cychosz K A, Thommes M, Su D, Stach E A, Ruoff R S (2011). Carbon-based supercapacitors produced by activation of graphene. *Science*, 332(6037): 1537–1541